Ultra-sensitive Transition-edge Sensors for Far-Infrared Spectroscopy on SPICA

A. D. Beyer[1,2], M. Kenyon[1,2], J. Bueno[1,2,3], P. M. Echternach[1,2], J.J. Bock[1,2], C.M. Bradford[1,2]
[1]*California Institute of Technology, Pasadena, CA 91125, USA*
[2]*Jet Propulsion Laboratory Pasadena, CA 91109, USA*
[3]*Currently at Centro de Astrobiologia (CSIC-INTA) Madrid, Spain*
*Contact: beyer@caltech.edu, phone 1-626-434-6868

Abstract—**We report progress in the fabrication of low-thermal conductance (G) transition-edge sensors (TESs) for SPICA. The TESs are silicon-nitride (Si-N) micro-mesh bolometers patterned into grid absorbers suspended by thin support beams. We are prototyping TESs for the Background Limited Far-Infrared Sub-millimeter Spectrograph (BLISS) far-infrared (IR) grating spectrometer, for which the photon-noise-limited noise-equivalent power (NEP) goal is 3×10^{-20}W/Hz$^{1/2}$ and the NEP requirement is 10^{-19}W/Hz$^{1/2}$. The NEP sets the thermal conductivity (G) for a 65 mK operating temperature to be G=4fW/K for the NEP goal and G=45fW/K for the NEP requirement. We report measurements of our progress toward meeting the requirement and goal G values. Additionally, BLISS requires the TESs to be sufficiently fast with an effective response time of $\tau_{eff} \leq$ 100ms. For the NEP requirement and G=45fW/K, the heat capacity (C) of the TES absorbers should be on the order of 10fJ/K, which we demonstrate here. In addition to building TESs and TES absorbers and support beams for BLISS, we can also manufacture TES absorbers and support beams suitable for the SpicA FAR-infrared Instrument (SAFARI). We investigate the effect of a dry XeF_2 etch versus a wet KOH etch on the C and G properties of BLISS-like and SAFARI-like absorbers and support beams.**

I. Introduction

Instrumentation and technology for infrared (IR) and sub-millimeter (mm) observations are enabling the next generation of investigations into the origins of galaxies, stars, planets, and life. In order to push forward the capabilities of far-IR/sub-mm spectroscopic instrumentation, we are building ultra-sensitive transition-edge sensors (TESs). Additionally, we are evaluating fabrication techniques for producing the absorbers, support beams, and bilayer thermistors, which are the building blocks of TESs. Our goal is to produce TESs suited to meet the requirements of the Background Limited far-Infrared/Sub-mm Spectrograph (BLISS). The fabrication techniques used to build the BLISS TESs could also be adapted to suit the SpicA FAR-infrared Instrument (SAFARI). Therefore, our TES detector technology is broadly designed for use with far-IR spectroscopy on the SPace Infrared telescope for Cosmology and Astrophysics (SPICA), a Japan Aerospace eXploration Agency (JAXA) led mission with ESA participation proposed for a 2018 launch.

II. BLISS Design

BLISS is a space-borne, broadband grating spectrometer used for far-IR/sub-mm spectroscopy. It is divided into five bands spanning 38μm-433μm. BLISS uses ultra-sensitive TESs as detectors. The detectors are required to exhibit a noise equivalent power NEP $=10^{-19}$ W/Hz$^{1/2}$, to have a fast effective response time $\tau_{eff} \leq$ 100ms, and to be scalable to more than 10^3 pixels. To be truly background limited, the NEP goal of BLISS is 3×10^{-20}W/Hz$^{1/2}$. The read out of the TES arrays is accomplished using a time-domain multiplexer scheme [1]. With $>10^3$ pixels in the current design, BLISS will have a resolving power of $R \equiv \lambda/\Delta\lambda \sim 700$ in each of the five bands. The combination of the goal NEP and resolving power $R \sim 700$ will allow observations that are background limited by the zodiacal and galactic cirrus diffuse astrophysical backgrounds in the far-IR/sub-mm spectrum.

The TESs use a membrane-isolated architecture consisting of a bilayer superconducting thermistor as the TES film, a mesh Si_xN_y (Si-N) absorber, and Si-N isolation legs suspending the bilayer and absorber from a Si-N on Si substrate. The architecture is shown in Fig. 1A. The bilayer thermistor is either a Mo/Au or Ti/Au bilayer, with the superconducting transition temperature T_C tuned by the proximity effect. We choose a value of T_C = 65mK because BLISS will utilize a space-qualified cryocooler capable of achieving a base temperature of 50mK.

The five bands of BLISS are designed to accommodate 1D or quasi-1D arrays of TESs to detect the output of the gratings in each band. The five bands and their span are listed in Table 1. A 1D array of TESs for the longest wavelength band fabricated at the Microdevices Laboratory (MDL) at the Jet Propulsion Laboratory (JPL) is shown in Fig. 1B. Fig. 1B illustrates the pixel dimensions Δx and Δy listed in Table 1 for the longest wavelength band of BLISS. The TESs are arranged in a 1D array to detect the outputs of machined gratings for the three longest wavelength bands of BLISS. This geometry is known as the WaFIRS geometry and has been utilized in Z-spec at the Caltech Submillimeter Observatory. The other two bands use quasi-1D arrays of TESs and cross-dispersed echelle grating modules to spread the incoming radiation out for detection. More details on the grating spectrometer design and echelle module design may be found in [2]. Ultimately, each TES in a given array will be read out by a time-domain Superconducting Quantum

Interference Device (SQUID) multiplexer (MUX). In this architecture, the wiring layer of the TESs runs from the TES films to the first-stage SQUID input coils in the MUX design [1].

The mesh absorbers on the TESs are designed to maximize the absorption of far-IR/sub-mm radiation. A schematic cross-section of the absorber architecture is shown in Fig. 1C. Each beam of the mesh absorber is suspended a distance x above the underlying substrate, and the substrate has a thickness denoted as y. The beams of the mesh absorber are a distance d apart, and a bilayer of Ti/Au with width w is deposited on top of the beams. The effective impedance of the absorber is given by $R_{eff}={}^{d}/_{w}\, R_F$, where R_F is the sheet resistance of the Ti/Au bilayer on top of the rungs. The Ti/Au thickness is tuned so that R_{eff} matches the impedance of the incoming radiation for maximal optical efficiency. A metal backshort at a distance of λ/4 is deposited on the backside of the Si underneath the absorber to increase optical coupling. The incoming radiation will be polarized parallel to the absorber beams to further enhance optical efficiency.

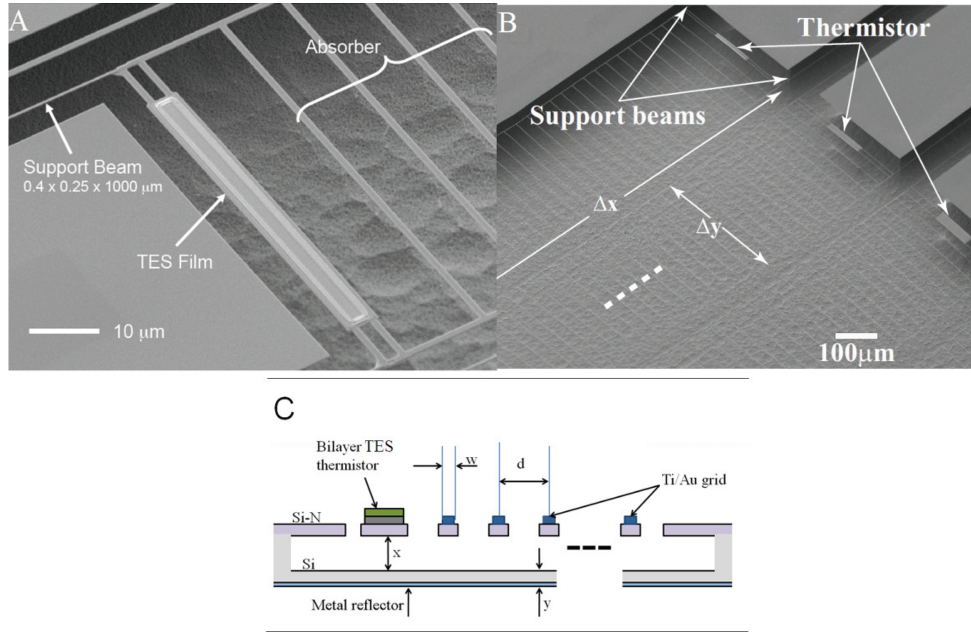

Fig. 1: BLISS TES and TES array: (A) Scanning electron microscope (SEM) image of a single BLISS TES in the longest wavelength band. The support beams, absorber, and TES film are shown. The TES is a bilayer thermistor of Mo/Au or Ti/Au for BLISS. (B) An SEM image of a 1D array of BLISS TESs in the longest wavelength band. The pixel dimensions Δx and Δy of Table 1 are illustrated here. (Figure reproduced from [5].) (C) Side-view schematic of a BLISS TES illustrating dimensions and components of the mesh absorbers. The height x and thickness y are controlled using double silicon-on-oxide (SOI) wafers.

TABLE 1: DIMENSIONS OF BLISS DETECTION BANDS

Band	λ_{min} (μm)	λ_{max} (μm)	Pixel Δx (μm)	Pixel Δy (μm)
1	38	67	306	193
2	67	116	535	337
3	116	180	873	140
4	180	280	1353	216
5	280	433	2097	336

The expected NEP due to the thermal impedance of the Si-N support beams is given by $NEP = \sqrt{4k_B T_C^2 G}$ [3]. Here k_B is Boltzmann's constant and G is the thermal conductance of the support beams. To meet the NEP requirement of BLISS, G should equal 45fW/K at the target T_C=65mK. To meet the NEP goal, G should equal 4fW/K at 65mK. The longest wavelength band shown in Fig. 1A has straight support beams 1mm long by 0.4μm wide by 0.25μm thick. The support beams for the three longest wavelength bands are straight beams, whereas the two remaining bands use meander beams in order to meet the different packing requirements for the quasi-1D arrays in the echelle modules.

The effective response time τ_{eff} goal of 100ms or less is dictated by the heat capacity C of the TES absorbers. The thermal time constant τ_0 = C/G, and

$$\tau_{eff} = \tau_0 \Big/ \left(1 + {}^{P_J \alpha}\!/_{G T_C}\right) , \qquad (1)$$

where P_J is the Joule power through the TES film and $\alpha = d\log R/d\log T$ is a measure of the sharpness of the superconducting transition. The value of τ_{eff} may be from 10-100 times smaller than τ_0 when the TES is voltage-biased in negative electrical thermal feedback (ETF) operation [4]. The time-domain MUX architecture will be voltage-biased to control the BLISS arrays; therefore, the BLISS goal for τ_{eff} will be met if C is between 45-450fJ/K for the NEP

requirement G of 45fW/K at 65mK. If G=4fW/K at 65mK for the NEP goal, C should be between 4-40fJ/K.

Modifications in the BLISS TES architecture can be made to produce TESs suitable for SAFARI, which is a Fourier transform spectrograph. The NEP and τ_{eff} requirements for the detectors on SAFARI are: NEP$\leq 10^{-19}$ W/Hz$^{1/2}$ and $\tau_{eff} \leq$ 10ms. Solid Si-N membrane absorbers are used instead of the mesh absorbers of BLISS, and the detectors are arranged in 2D arrays. The slightly higher NEP goal permits thicker support beams to be used in a membrane-isolation TES structure. Given the NEP goal, the value of G should be less than or equal to 45fW/K at 65mK. Assuming a 10-100 reduction in τ_{eff} compared to τ_0, C will need to be on the order of 1fJ/K for SAFARI TESs.

III. Fabrication

A. Composite BLISS TESs

Micromachining and lithographic patterning processes are used to produce TESs. Each TES consists of a bilayer thermistor, a Si-N absorber, Si-N support beams, a wiring layer, and a substrate supporting the membrane-isolated TES. The TESs are constructed at JPL using 100mm <100> Si wafers. In the future, the TESs will be fabricated using double silicon-on-oxide (SOI) wafers. Silicon-oxide (SiO_2) layers buried in the SOI wafers will be used to control the front and backside etch depths, shown as dimensions x and y in Fig. 1C.

A layer of low-stress Si-N with controllable thickness is first grown on top of a wafer using low pressure chemical vapor deposition. Low stress is important to prevent warping of the Si-N structures when the Si underneath them is released. The silicon underneath the Si-N structures is removed using a dry XeF_2 gas-etch or a wet KOH etch. A layer of photoresist (PR) is used to protect the top Si-N surfaces from the etchants. The PR is cleaned off after the devices are released from the silicon underneath the Si-N. Additionally, a layer of SiO_2 left behind from the growth of Si-N protects the underside of the Si-N for the devices prepared using a dry XeF_2 gas-etch.

The thermistor consists of a bilayer of Mo/Au or Ti/Au deposited onto the Si-N, and the wiring layer is deposited on top of the Mo/Au or Ti/Au thermistor and runs along the support beams to bond pads. Additionally, the size of the thermistor is patterned to produce a thermistor with the desired normal state resistance to match the designs of the time-domain multiplexer for controlling the TES arrays.

B. Si-N Test Structures for BLISS and SAFARI

The NEP and τ_{eff} for BLISS and SAFARI depend strongly on the values of G and C that can be obtained from the Si-N absorbers and support beams. Therefore, we have fabricated noise thermometry test devices that can be used to test the effect of different fabrication processes on the value of G and C for BLISS-like and SAFARI-like absorber and support beam architectures. Our BLISS-like noise thermometry device has support beams with a cross section that is typically 0.25um thick by 0.4um wide, and the absorber is a micromesh grid absorber with fill factor of 10%, as shown in Fig. 2A. The rungs are 1μm wide and are spaced 10μm apart for this absorber. In contrast, our SAFARI-like noise thermometry device has larger cross section support beams that are typically 1μm thick and 5μm wide. The SAFARI-like absorber is a solid membrane absorber, as shown in Fig. 2B, and it is 1μm thick.

The SAFARI-like noise thermometry devices are released using either a dry XeF_2 etch or a wet KOH etch, whereas the narrow beams and spider-web like structure for the BLISS-like devices have been fabricated using the XeF_2 release process. In the mesh-absorber design for BLISS TESs, wet etching could result in the absorber and support beams becoming stuck together. Additionally, the absorbers and support beams could break from a wet etch process. Future designs to prevent the sticking and breaking of beams could incorporate additional Si-N separation beams. The separation beams would keep the support and absorber beams apart and prevent breakage. The separation beams could later be removed by cutting them with a laser.

The layer of PR that protects the top surfaces of the noise thermometry devices during etching is removed by either an O_2 deep reactive ion etch (DRIE) or by rinsing in warm isopropyl alcohol and acetone. The mesh absorber has SiO_2 underneath the Si-N, while the solid absorber does not.

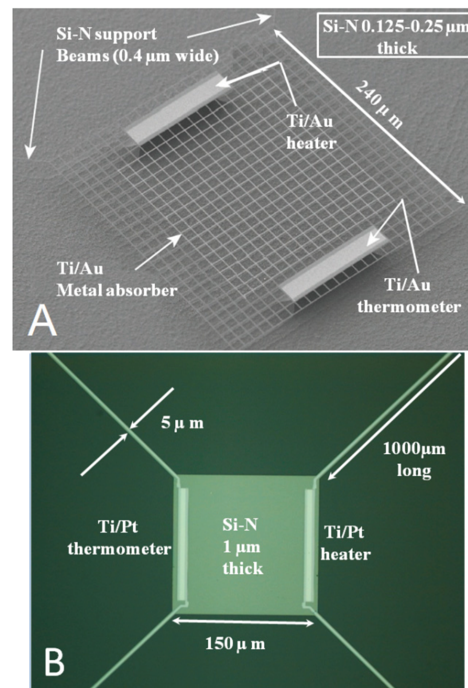

Fig. 2: SEM images of noise thermometry devices for determining thermal properties of Si-N: (A) The BLISS-like noise thermometry absorber device. The support beams are typically 0.4μm wide × 0.25μm thick × 1000μm long. The mesh has a 10% fill factor. (Image reproduced from [5].) (B) The solid membrane noise thermometry absorber device has support beams that are 5μm wide × 1μm thick × 1000μm long. The support beams and solid membrane absorber reproduce an architecture used in SAFARI TESs.

Two resistors composed of Ti/Pt or Ti/Au are lithographically defined on opposite sides of the noise thermometry devices to provide resistors. The resistors are used as a heater and a thermometer. The heater is hooked up to a current source, and the thermometer is wired up to a SQUID input coil to measure the current noise of the resistor. A wiring layer is deposited on top of the resistors to provide electrical links to the SQUID and bias line, with the wiring layer running along the support beams.

IV. Experimental procedure

We measured C and G values for the two noise thermometry devices in a ^{3}He-^{4}He Janis dilution refrigerator with a base temperature of 15mK. The devices were mounted onto a gold-plated copper plate attached to the mixing chamber of the refrigerator and surrounded by an enclosed Nb shielding can. The thermometer was connected by wire bonds to NbTi superconducting wires. The NbTi wires passed through Nb capillaries to the input coil of a SQUID for readout of the thermometer current response and power spectral density. The heater resistor was connected via wire bonds to a lossy coaxial bias line connection.

The Nb can served to prevent optical dark power from reaching the test devices and to shield from magnetic pickup. To pump out any excess ^{3}He exchange gas or air inside the Nb can, we employed a meandered pump-out port filled with bronze mesh. The bronze mesh served to prevent optical dark power from leaking through the pump-out port to the devices, while still maintaining throughput for pump-out.

Attenuators, filters, and lossy coaxial cables helped to prevent electrical dark power from passing down the bias line to the device, as shown in Fig. 3A. Lossy coaxial cables were inserted between the room temperature bias input port and the device input port. We also inserted a 30dB or 30dB+10dB attenuator in series at the 1K pot stage between the coaxial cable from room temperature and the device. Two mini-circuits low-pass filters with roll-off at 300 MHz and 1.9 MHz were inserted into the lossy coaxial line prior to connection to the device. The mini-circuits were held at the mixing chamber temperature T_{mx}.

The thermometer resistance was calibrated by varying T_{mx} and observing the Johnson noise current detected by the SQUID. The electron temperature can be calculated from the Johnson noise current formula

$$S_I = 4k_B T_e / R_{th} \ , \qquad (2)$$

where T_e is the electron temperature, R_{th} is the thermometer resistance, and S_I is the power spectral density of the Johnson noise current sensed by the SQUID.

Experimentally, the thermal conductance G is determined by applying a small change in bias power to the heater resistor and measuring the resulting ΔT on the thermometer for a fixed T_{mx}. Quantitatively, $G = \Delta P / \Delta T$. Here ΔP is the small change in bias power.

If no dark power P_D reaches the noise thermometry devices, a linear relationship between T_{mx} and T_e will be observed at all temperatures. Any dark power P_D impinging upon the device will cause a deviation in T_e from T_{mx}. The expected deviation is

$$T_e - T_{mx} \approx P_D / G(T_{mx}). \qquad (3)$$

Given the small G values of the noise thermometry devices and TESs, the dark power would ideally be below 1fW. Using all the measures described above, we found the dark power was around 0.22fW for a 30dB+10dB or 0.6fW for a 30dB attenuator in our experimental setup, as shown in Fig. 3B.

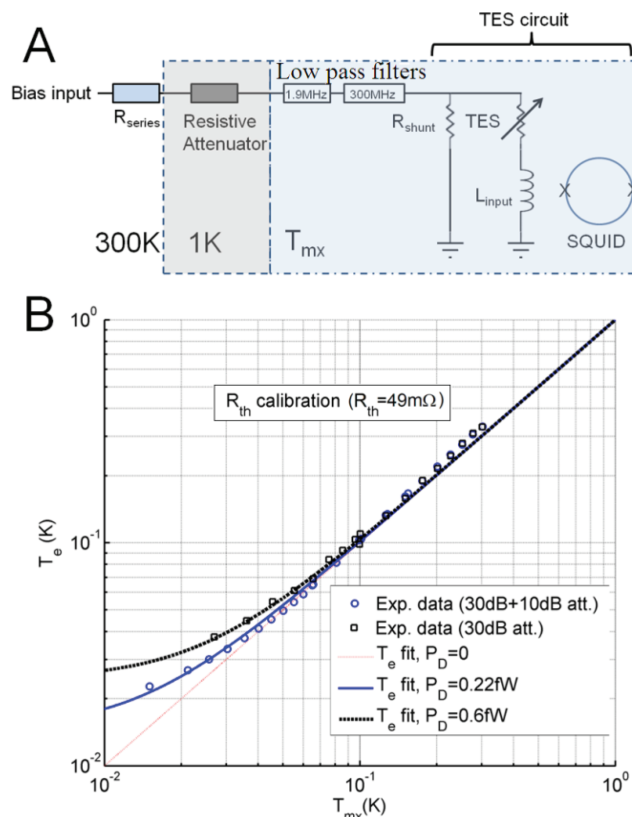

Fig. 3: (A) Experimental setup for noise thermometry measurements. (B) Measurement of electron temperature T_e vs. mixing chamber temperature T_{mx}. The dark power is below 1fW in our experimental setup.

Once the values of G(T) are determined, C(T) is measured by applying a small heat pulse to the heater resistor and observing the decay time τ_0 at different mixing chamber temperatures. The measurement is operated without ETF; therefore, $C(T)=\tau_0(T)\times G(T)$.

V. Results and discussion

Table 2 shows thermal and performance properties obtained from our measurements of the two Si-N absorber geometries prepared under different fabrication techniques at T=100mK .

In addition, we have included Si-N properties obtained from similar geometries for comparison in the literature [5]-[7]. The values shown for [5] are for T=60mK, and the values shown for [7] are for T=113mK. To obtain the NEP values at T=65mK, the values of G have been extrapolated to T=65mK using $G\sim T^{1/2}$ for mesh absorbers [5] and $G\sim T^{3/2}$ for solid absorbers.

TABLE 2: THERMAL PROPERTIES OF Si-N AT 100MK

A comparison of the Si-N heat capacity (C), surface specific heat (c_S), thermal conductance (G), expected heat capacities for bands 3-5 of BLISS, and estimated thermal time constant τ_0 in band 4 (based on the assumption of G=4fW/K). We prepared mesh-absorber BLISS-like noise thermometry devices (Fig.2A) and solid-membrane-absorber SAFARI-like noise thermometry devices (Fig.2B) using different fabrication processes. Selected results from the literature are also included for comparison.

No.	Type	Process	Bilayer (nm/nm)	G (fW/K)	C_{SiN} (fJ/K)	c_S (aJ/[K·µm^2])	$C_{Band\ 3}$ (fJ/K)	$C_{Band\ 4}$ (fJ/K)	$C_{Band\ 5}$ (fJ/K)	τ_0 (Band 4) (s)	NEP (W/Hz$^{1/2}$) at 65mK
1	Solid	wet KOH etch; *IPA/Acetone*	Ti/Pt (2/50)	1500	3	0.04	1.0	1.5	2.4	0.39	4.3×10^{-19}
2	Solid	wet KOH etch; *IPA/Acetone*	Ti/Pt (2/50)	1000	6	0.08	2.0	3.1	4.8	0.77	3.5×10^{-19}
3	Solid	XeF_2 dry etch; *O_2 DRIE*	Ti/Pt (2/50)	450	146	1.98	50.0	76.5	119	19.12	2.3×10^{-19}
4	Solid	XeF_2 dry etch; *IPA//Acetone*	Ti/Pt (2/50)	1000	171	2.32	58.5	89.6	139	22.40	3.5×10^{-19}
5	Mesh	XeF_2 dry etch; IPA/Acetone +O_2 DRIE	Ti/Au (2/50)	130	89	3.06	77.2	118.2	184	29.55	1.6×10^{-19}
[5]	Mesh	XeF_2 dry etch; *O_2 DRIE*	Ti/Au (2/50)	54	98	3.98	100.4	153.7	239	38.43	1.1×10^{-19}
[6]	Solid	DRIE	Mo/Au	5500	50	1.02	25.7	39.4	61.2	9.85	8.2×10^{-19}
[7]	Solid	wet KOH etch	Ti/Au	320	1.4	0.03	0.8	1.2	1.8	0.29	1.8×10^{-19}

Due to the fact that metals have a larger specific heat than Si-N, we have calculated the heat capacity contribution $C_{bilayer}$ of the different bilayers to the total heat capacity, C_{tot}. We obtained the heat capacity of the Si-N according to $C_{Si-N}=C_{tot}-C_{bilayer}$. To calculate $C_{bilayer}$, we used γ_{Ti}=3.35mJ/(mol·K^2), γ_{Au}=0.729mJ/(mol·K^2), and γ_{Pt}=6.8mJ/(mol·K^2) [8].

The NEPs shown in Table II are expected to be on the order of 10^{-19}W/Hz$^{1/2}$ for T_C=65mK for both solid and mesh devices based on the values of G. Despite the scatter in G values for the solid devices, the values are consistently on the order of 10-100fW/K—except for the solid device in [6]. This device is connected to the substrate bath via perforations in the Si-N, which explains the larger value of G, and is designed for soft X-ray spectroscopy instead of far-IR spectroscopy. The mesh devices have smaller G values than the solid devices because their support beams are thinner than those of the solid devices. Device 5 and the average result from mesh devices in [5] differ in G because the support beams were twice as long in [5] as in device 5. Taking all these factors into consideration, neither the etchant nor the PR removal steps affect G much. As can be seen, G is converging toward the BLISS/SAFARI requirements.

The strongest effects due to process can be seen in the values of C in Table 2. The values of C for the wet etch are on the order of 1fW/K at 65mK, whereas the C values for the XeF_2 etch are on the order of 10-100fW/K for both solid and mesh absorbers. Table 2 indicates that the type of process for removing PR did not change the C values significantly for either type of absorber; therefore, we conjecture that the differences are due to the type of etchant based on the solid membrane results. Wet KOH etching seems to produce solid membranes with lower C than XeF_2.

As described in the Section III, we have not produced mesh devices using the wet etch process. However, mesh devices prepared using XeF_2 showed similar values of C to solid absorber devices. This result is surprising because the surface area of solid absorbers is 45,600µm^2, whereas that of the mesh absorbers is 28,275µm^2. A simple scaling of surface area would predict a smaller value of C in mesh devices.

The values of C for the solid and mesh absorbers etched with XeF_2 could be similar if the edges and top/bottom surfaces of the devices have different specific heat values per surface area. (It has been shown that the Si-N thickness does not affect C for mesh devices [5].) This scenario could result because the top and bottom surfaces of the devices were protected during XeF_2 etching, whereas the edges were not. Using the values of C from devices 4 and 5 and the edge and top/bottom surface areas, we calculate the edge specific heat to be 6.5aJ/µm^2 and the top/bottom surface specific heat to be 2aJ/µm^2. Both results are on the order of 1aJ/µm^2, similar to a value observed in [9]. The interaction of XeF_2 with the SiO_2 protecting the bottom surface of the mesh devices could also explain the discrepancy.

For the solid membrane devices, we estimate the specific heat to be 0.1aJ/µm^2 by ignoring the edges. This value is the same order of magnitude of specific heat expected for

amorphous materials such as vitreous silica, which has a specific heat equal to 0.22aJ/μm^2 [10].

We can then conjecture that the use of XeF_2 is correlated with added C in our investigation. Randomly distributed populations of two-level systems explain the specific heat values observed in amorphous materials, such as vitreous silica [11]. Therefore, it is possible that the XeF_2 is introducing additional TLS into our Si-N, possibly through diffusion of F_2 into the Si-N. Again, the XeF_2 interacting with SiO_2 could also be responsible for the excess specific heat. For T>1K, the type of SiO_2 used as a substrate for growing Si-N does affect the specific heat of Si-N produced [12]. Different SiO_2 growth techniques and the interaction with XeF_2 could be investigated. However, our values of C differ by two orders of magnitude devices from Si-N grown in the same way. Therefore, the major difference appears to be due to the type of etch. We are continuing to investigate these issues, but we find that the C values measured are within the requirements for far-IR spectroscopy instruments on SPICA, such as BLISS or SAFARI.

VI. Conclusions

Meeting the demands of far-IR spectroscopy detectors for SPICA requires TES detectors with G and C values to meet the NEP=10^{-19}W/Hz$^{1/2}$ requirement and $\tau_{eff} \leq 100$ms requirements. Our values of G are approaching the 45fW/K needed to meet the requirement NEPs of BLISS and SAFARI at 65mK, and we are developing methods to reach the NEP goal of 3×10^{-20}W/Hz$^{1/2}$ for BLISS. Our demonstrated values of C for the mesh-absorber noise thermometry devices are on the order of 10fJ/K, which is necessary to meet the τ_{eff} requirement for TESs on BLISS. Similarly, the demonstrated values of C for the solid-membrane-absorber noise thermometry devices are on the order of the 1fJ/K, which is necessary to meet the τ_{eff} requirements for TESs on SAFARI. Finally, we may be able to reduce C further for BLISS TESs with different fabrication techniques.

Acknowledgment

A.D. Beyer thanks the Caltech Moore Foundation for financial support. This research was carried out at the Jet Propulsion Laboratory, California Institute of Technology, under a contract with the National Aeronautics and Space Administration.

© 2010 California Institute of Technology. Government sponsorship acknowledged.

References

[1] Piet. A.J. de Korte *et al.*, "Time-division superconducting quantum interference device multiplexer for transition-edge sensors," *Rev. Sci. Instr.*, Vol. 74, pp. 3807-3815. Aug. 2003.

[2] C.M. Bradford *et al.*, "BLISS for SPICA: Far-IR at the background limit," in *Vol. 375*, *Proc. of From Z-Machines to ALMA: (Sub)Millimeter Spectroscopy of Galaxies Conference (SPIE)*, Charlottesville, Virginia, United States, 2006, pp. 199-210.

[3] J. C. Mather, "Bolometer noise: nonequilibrium power" *Applied Optics*, Vol. 21, pp. 1125-1129. March 1982.

[4] K.D. Irwin, "An application of electrothermal feedback for high resolution cryogenic particle detection," *App. Phys. Lett.* , Vol. 66, pp. 1998-2000. April 1995.

[5] M. Kenyon, P.K. Day, C.M. Bradford, J.J. Bock, and H.G. Leduc, "Ultra-sensitive transition-edge sensors (TESs) for space-borne far-IR/submm spectroscopy," *Proc. of 13th International Workshop on Low-Temperature Detectors*, Stanford, California, United States, 2009, pp. 56-59.

[6] Megan E. Eckart *et al.*, "Experimental results and modeling of low-heat-capacity TES Microcalorimeters for Soft-X-ray Spectroscopy," *Proc. of 13th International Workshop on Low-Temperature Detectors*, Stanford, California, United States, 2009, pp. 430-433.

[7] P. Khosropanah *et al.*, "Low Thermal Conductance Transition Edge Sensor (TES) for SPICA," *Proc. of 13th International Workshop on Low-Temperature Detectors*, Stanford, California, United States, 2009, pp. 42-47.

[8] Charles Kittel, *Introduction to Solid State Physics*, Sixth edition. New York: John Wiley & Sons, Inc. 1986, pg. 141.

[9] Warren A. Holmes *et al.*, "Initial test results on bolometers for the Planck high frequency instrument," *Applied Optics*, Vol. 47, pp. 5996-6008. Nov. 2008.

[10] R. C. Zeller, R.O. Pohl, "Thermal conductivity and specific heat of noncrystalline solids," *Phys. Rev. B.*, Vol. 4, pp. 2029-2041. May 1971.

[11] W.A. Phillips, "Two-level states in glasses," *Rep. Prog. Phys.* Vol. 50, pp. 1657-1708. Feb. 1987.

[12] B.L. Zink, F. Hellman, "Specific heat and thermal conductivity of low-stress amorphous Si-N membranes," *Solid State Comm.* Vol. 129, pp. 199-204. Jan. 2004.